

## THE DISTANCE AND MASS OF THE GALAXY CLUSTER ABELL 1995 DERIVED FROM SUNYAEV-ZELDOVICH EFFECT AND X-RAY MEASUREMENTS

SANDEEP K. PATEL<sup>1</sup> AND MARSHALL JOY

Department of Space Science, SD50 NASA Marshall Space Flight Center Huntsville, AL 35812

JOHN E. CARLSTROM, GILBERT P. HOLDER, AND ERIK D. REESE

Department of Astronomy and Astrophysics, University of Chicago, Chicago, IL 60637

PERCY L. GOMEZ AND JOHN P. HUGHES<sup>2</sup>

Department of Physics and Astronomy, Rutgers University, 136 Frelinghuysen Road, Piscataway, NJ 08854-8019

LAURA GREGO

Harvard-Smithsonian Center for Astrophysics, 60 Garden Street, Cambridge, MA 02138

AND

WILLIAM L. HOLZAPFEL

Department of Physics, University of California Berkeley, Berkeley, CA 94720

Received 2000 January 12; accepted 2000 April 4

### ABSTRACT

We present multiwavelength observations of the Abell 1995 galaxy cluster. From an analysis of X-ray spectroscopy and imaging data, we derive the electron temperature, cluster core radius, and central electron number density. Using optical spectroscopy of 15 cluster members, we derive an accurate cluster redshift and velocity dispersion. Finally, the interferometric imaging of the Sunyaev-Zeldovich effect toward Abell 1995 at 28.5 GHz provides a measure of the integrated pressure through the cluster. The X-ray and Sunyaev-Zeldovich effect observations are combined to determine the angular diameter distance to the cluster of  $D_A = 1294^{+294}_{-283} +^{438}_{-458}$  Mpc (statistical followed by systematic uncertainty), implying a Hubble constant of  $H_0 = 52.2^{+11.4}_{-11.9} +^{18.5}_{-17.7}$  km s<sup>-1</sup> Mpc<sup>-1</sup> for  $\Omega_M = 0.3$  and  $\Omega_\Lambda = 0.7$ . We find a best-fit  $H_0$  of 46 km s<sup>-1</sup> Mpc<sup>-1</sup> for the  $\Omega_M = 1$  and  $\Omega_\Lambda = 0$  cosmology, and 48 km s<sup>-1</sup> Mpc<sup>-1</sup> for  $\Omega_M = 0.3$  and  $\Omega_\Lambda = 0.0$ . The X-ray data are also used to derive a total cluster mass of  $M_{\text{tot}}^{\text{HSE}}(r_{500}) = 5.18^{+0.62}_{-0.48} \times 10^{14} h^{-1} M_\odot$ ; the optical velocity dispersion yields an independent and consistent estimate of  $M_{\text{tot}}^{\text{virial}}(r_{500}) = 6.35^{+1.51}_{-1.19} \times 10^{14} h^{-1} M_\odot$ . Both of the total mass estimates are evaluated at a fiducial radius,  $r_{500} = 830 h^{-1}$  kpc, where the overdensity is 500 times the critical density. The total cluster mass is then combined with gas mass measurements to determine a cluster gas mass fraction of  $f_g = 0.056^{+0.010}_{-0.013} h^{-3/2}$ . In combination with recent baryon density constraints, the measured gas mass fraction yields an upper limit on the mass density parameter of  $\Omega_M h^{1/2} \leq 0.34^{+0.06}_{-0.05}$ .

*Subject headings:* cosmology: observations — dark matter — distance scale — galaxies: clusters: individual (Abell 1995) — X-rays: general

### 1. INTRODUCTION

Clusters of galaxies are among the most massive and X-ray luminous objects in the universe. The source of this X-ray emission is the hot ( $\sim 10^8$  K) plasma that is bound in the gravitational potential of the cluster and radiates primarily by thermal bremsstrahlung. In addition, this high-temperature plasma interacts with the cosmic microwave background (CMB) radiation field via the inverse-Compton process (the Sunyaev-Zeldovich effect [SZE]), producing an increment in intensity at frequencies higher than  $\sim 218$  GHz, and an intensity decrement at lower frequencies (Sunyaev & Zeldovich 1972, 1980; Rephaeli 1995; Birkinshaw 1999).

In this paper, we present X-ray imaging and spectroscopy, interferometric imaging of the SZE, and optical spectroscopy of Abell 1995, a massive galaxy cluster at a redshift of  $\sim 0.3$ . These measurements are used to determine several physical parameters of the cluster: an accurate redshift, velocity dispersion, electron temperature, SZE decrement,

and central electron density. The X-ray and SZE observations are combined to determine the cluster distance, and hence yield a measure of the Hubble constant,  $H_0$  (for a recent review see Birkinshaw 1999). The X-ray data and optical velocity dispersion are also used to derive independent and consistent estimates of the total mass of the cluster, which are then combined with gas-mass measurements to place constraints on the cluster gas mass fraction and baryon fraction.

The observational data for Abell 1995 (X-ray imaging and spectroscopic observations from *ROSAT* and *ASCA*, imaging of the SZE at the Berkeley-Illinois-Maryland Association [BIMA] and Owens Valley Radio Observatory [OVRO] millimeter-wave interferometers, and optical spectroscopy obtained at the Multiple Mirror Telescope [MMT]<sup>3</sup>) are presented in § 2. The cluster distance analysis is presented in § 3, and the cluster mass and baryon fraction analysis is found in § 4. Finally, in § 5 we summarize our conclusions and discuss the improvements expected from the upcoming *Chandra X-Ray Observatory* measurements of Abell 1995.

<sup>1</sup> Department of Physics, University of Alabama in Huntsville, Huntsville, AL 35899.

<sup>2</sup> Service d'Astrophysique, L'Orme des Merisiers, CEA-Saclay, 91191 Gif-sur-Yvette Cedex, France.

<sup>3</sup> The Multiple Mirror Telescope is a joint facility of the Smithsonian Institution and the University of Arizona.

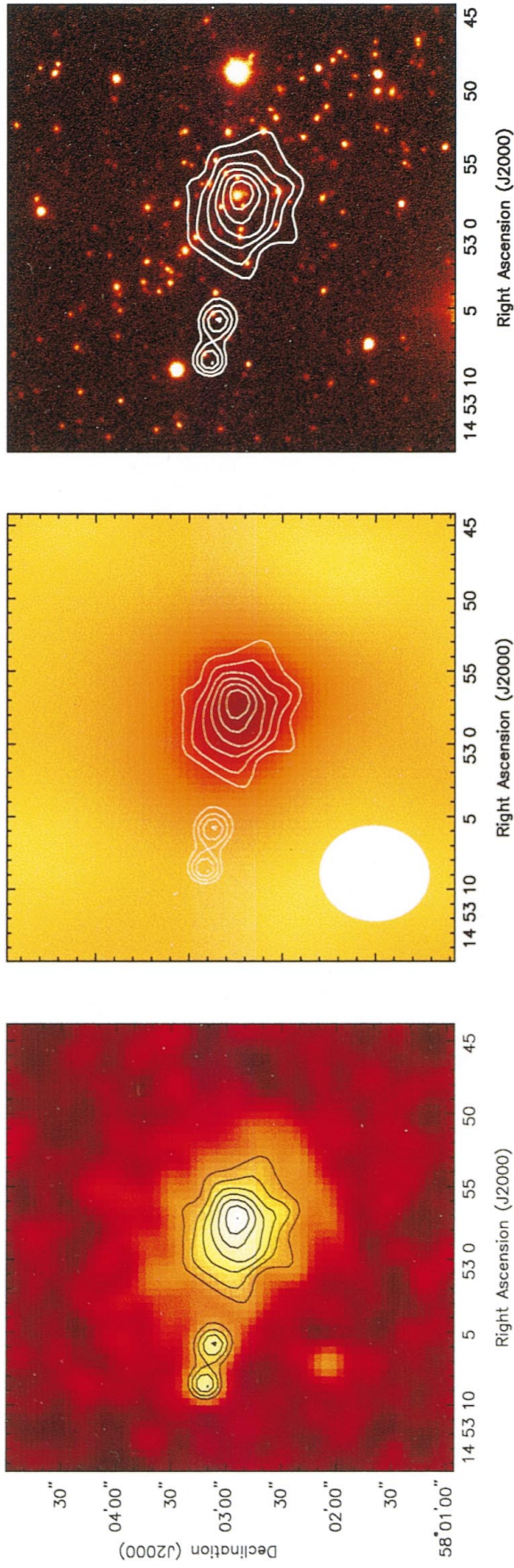


FIG. 1.—(a) Central portion of the PHA-filtered *ROSAT* HRI X-ray image of Abell 1995 smoothed using a Gaussian function with  $\sigma = 6''$ . The false-color scale represents the number of counts detected. The peak surface brightness is  $3.32 \times 10^{-2}$  HRI counts  $s^{-1} \text{ arcmin}^{-2}$ , and the contours are at 40%, 50%, 60%, 70%, 80%, and 90% of the peak. The three X-ray point sources located  $\sim 1.5$  to the east and southeast of the cluster have been excluded in the analysis of the HRI data. (b) Cleaned SZE map of Abell 1995 observed at OVRO, shown in false color with X-ray contours superimposed. The restoring beam has a Gaussian FWHM of  $51.96 \times 58.88$  and an rms noise of  $\sim 55 \mu\text{Jy beam}^{-1}$ , corresponding to a RJ brightness sensitivity of  $\sim 27 \mu\text{K}$ . The SZE image presented here was produced with a Gaussian ( $u, v$ ) taper of 0.5 at  $2.0 \text{ k}\lambda$ . (c) Whipple Observatory 1.2 m R-band image of Abell 1995, shown in false color with X-ray contours superimposed. The X-ray center is coincident with the cD galaxy 1451 + 581.5B (Huchra et al. 1990; galaxy 5 in Table 4 of this paper).

Throughout this paper we parameterize the Hubble constant in terms of  $h$ , where  $H_0 \equiv 100 h \text{ km s}^{-1} \text{ Mpc}^{-1}$ . Uncertainties are reported at the 68% confidence level, and a cosmology of  $\Omega_M = 0.3$  and  $\Omega_\Lambda = 0.7$  is used unless explicitly stated otherwise.

## 2. OBSERVATIONS AND ANALYSIS

### 2.1. X-Ray Imaging

Abell 1995 was observed with the *ROSAT* High-Resolution Imager (HRI) on 1994 July 30, 1995 January 20, and 1995 November 13 for a combined live time of 37,571 s. We use these data to constrain the spatial structure of this cluster. The HRI data reduction was done using the IRAF/PROS image-analysis package. The data from the individual pointings of Abell 1995 were combined, after checking that there were no positional offsets between them. In order to reduce the background (David et al. 1997), the data were filtered to include only pulse-height channels 1–7, resulting in a total of  $1911 \pm 210$  background-subtracted events detected within a circular region  $5'$  in radius centered on the cluster. The resulting X-ray image is shown in Figure 1a. The X-ray peak coincides with a galaxy whose J2000 coordinates are  $\alpha = 14^{\text{h}}52^{\text{m}}57^{\text{s}}.45$ ,  $\delta = +58^{\circ}02'55''.2$  (see § 4). Overlaid on all the images in Figure 1 are the HRI surface brightness contours smoothed with a  $\sigma = 6''$  Gaussian in increments of 10% of the peak brightness.

The pulse-height-filtered HRI data were blocked by a factor of 16 into  $8'' \times 8''$  pixels, and the resulting image fitted using a robust downhill simplex method that maximizes a likelihood function  $L$ , which is the product of the individual Poisson probabilities over all pixels in the region of the image being fitted. To determine the best-fit parameters, we construct and minimize a  $\chi^2$ -like statistic,  $S \equiv -2 \ln L$ , which is equivalent to maximizing  $L$  (Cash 1979; Kendall & Stuart 1979; Hughes & Birkinshaw 1998). To describe the density distribution of the X-ray-emitting gas, we use a spherical  $\beta$  model (Cavaliere & Fusco-Femiano 1976, 1978),

$$n_e(\theta) = n_{e0} \left( 1 + \frac{\theta^2}{\theta_c^2} \right)^{-3\beta/2}, \quad (1)$$

where  $n_{e0}$  is the central electron density,  $\theta_c$  is the angular core radius, and  $\beta$  is the parameter that describes the radial falloff of the gas distribution. We determine the parameters  $\beta$  and  $\theta_c$  by fitting the X-ray surface brightness data to the function

$$S_X(\theta) = S_{X0} \left( 1 + \frac{\theta^2}{\theta_c^2} \right)^{-3\beta+1/2} + B, \quad (2)$$

where the first term follows directly from the line-of-sight integration of the X-ray emissivity, where  $S_{X0}$  is the central X-ray surface brightness and  $B$  is the X-ray background, assumed to be spatially uniform across the central area of the detector.

We convolve the surface brightness model (eq. [2]) with the on-axis point-response function of the combined telescope/detector system using the parameterization given by David et al. (1997). Fits were done over a restricted portion of the field of view, a circular region with radius  $5'$  ( $0.98 h^{-1} \text{ Mpc}$ ) centered on the position of the peak cluster emission. X-ray point sources in the field were excluded from the analysis. The best fit is obtained by allowing all

parameters of the model ( $\beta$ ,  $\theta_c$ ,  $S_{X0}$ ,  $B$ , and position) to vary freely. The best-fit background level is  $B = 3 \times 10^{-3} \text{ HRI counts s}^{-1} \text{ arcmin}^{-2}$ , which is within the expected range (David et al. 1997) and consistent with the background level estimated from an annular region surrounding the cluster, outside the fitted region. The best-fit position of the X-ray cluster center is  $\alpha = 14^{\text{h}}52^{\text{m}}57^{\text{s}}.8$ ,  $\delta = 58^{\circ}02'54''.3$  (J2000). The best-fit spherical  $\beta$  model parameters are  $\beta = 0.672^{+0.052}_{-0.035}$ ,  $\theta_c = 32''.5^{+2''.9}_{-4''.3}$ , and  $S_{X0} = 3.24^{+0.39}_{-0.14} \times 10^{-2} \text{ counts s}^{-1} \text{ arcmin}^{-2}$ . The statistical uncertainties quoted here are the one-dimensional confidence interval for each parameter corresponding to  $\Delta\chi^2 = 1$ , where  $\Delta\chi^2 \equiv S - S_{\text{min}}$ , while all other parameters are free to assume their best-fit values.

To evaluate the uncertainty in the cluster distance due to statistical variations in the fitted model parameters, we create a grid in  $(\theta_c, \beta)$  space with ranges of  $0.50 \leq \beta \leq 0.90$  and  $18'' \leq \theta_c \leq 60''$ . Each point in this grid is fitted to the X-ray data to determine the central X-ray surface brightness and an associated  $\Delta\chi^2$  value. The joint confidence regions for  $\theta_c$  and  $\beta$  are shown in Figure 2.

### 2.2. X-Ray Spectroscopy

Abell 1995 was observed by *ASCA* on 1994 June 12–13. On board *ASCA* are four independent X-ray telescopes and four independent X-ray detectors: two Gas Imaging Spectrometers (GISs) and two Solid State Imaging Spectrometers (SISs). For this analysis, we have included all available *ASCA* data sets. These data sets were extracted from the *ASCA* archive at the High-Energy Astrophysics Science Archive Research Center, and the standard screening cri-

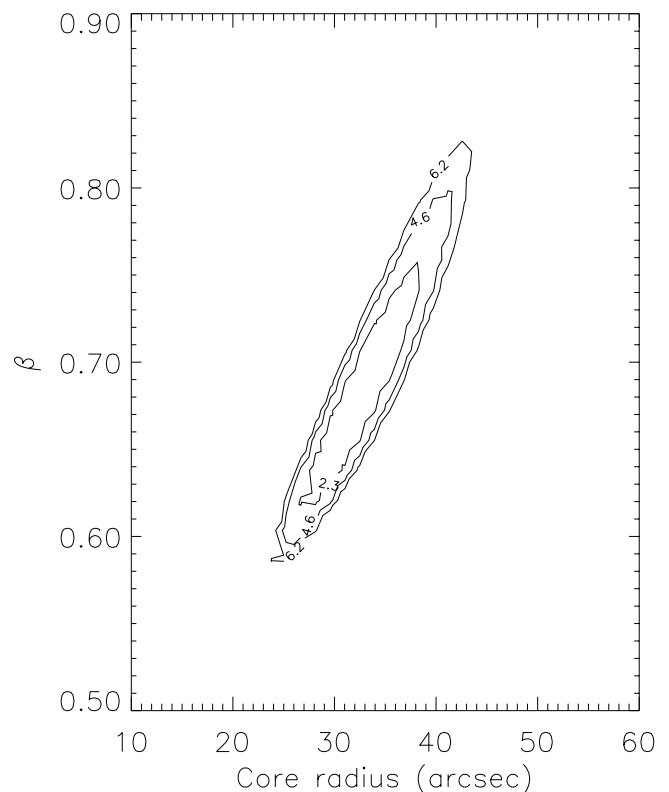


FIG. 2.—Confidence-level contours for isothermal  $\beta$  model fits to the *ROSAT* HRI image of Abell 1995. The  $\Delta\chi^2$  contour levels are 2.3, 4.6, and 6.2, which correspond to the 68.3%, 90%, and 95.4% confidence levels for two free parameters.

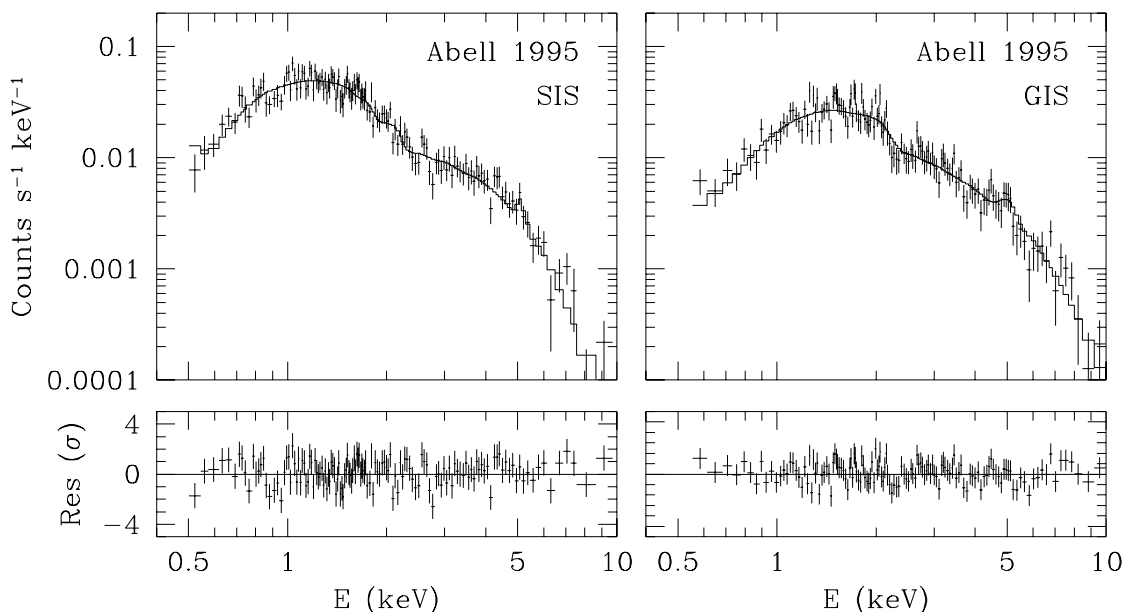


FIG. 3.—*ASCA* SIS and GIS spectral data, best-fit models, and residuals (in units of  $\sigma$ ). The spectrum was fitted with a Raymond-Smith thermal emission model with the temperature, abundance, and Galactic absorption allowed to vary. The best-fit values for the cluster gas temperature, abundance, and absorbing column density are presented in Table 2.

teria (Day et al. 1995) were applied. Data reduction was carried out separately for each GIS detector and for each SIS detector in both 1-CCD and 4-CCD modes. Spectra were taken from a circular region centered on the cluster with a radius of  $4'$  for the SIS data and  $5.4'$  for the GIS data. A smaller region than the recommended  $6'$  was used for the GIS in order to avoid an unresolved X-ray source to the northeast. Background was taken from *ASCA* observations of several high Galactic latitude fields, obtained from the *ASCA* Guest Observers Facility, using similar data screening criteria and with obvious X-ray point sources removed. The background was statistically well determined with rates of  $0.021 \text{ s}^{-1}$  (SIS0 and SIS1),  $0.017 \text{ s}^{-1}$  (GIS2), and  $0.019 \text{ s}^{-1}$  (GIS3). Table 1 gives the resulting background-subtracted count rates and effective exposure times. Response files were generated (using FTOOLS tasks *ascaarf* and *sisrmg*) for each detector and mode of operation separately. For spectral analysis, all the SIS data were combined into a single data set, as were the GIS data, in each case weighting the response functions by their individual effective live times. The data were grouped into energy channels that contained at least 25 events each. The resulting *ASCA* data were used to constrain the spectral properties of the hot intracluster plasma in the cluster, i.e., the metallicity and temperature. A joint fit to the SIS and GIS data (using

XSPEC version 10) of a Raymond & Smith (1977) thermal plasma spectral model including the effects of Galactic absorption gave a good fit, with a  $\chi^2$  of 273.3 for 273 degrees of freedom (Fig. 3). This fit results in a temperature of  $8.59^{+0.86}_{-0.67} \text{ keV}$  and a fractional metal abundance of  $0.14 \pm 0.07$  solar (Table 2). Mushotzky & Scharf (1997) derived a somewhat higher temperature ( $10.7 \text{ keV}$ , 90% confidence interval  $8.9\text{--}13.2 \text{ keV}$ ); however, the metal abundance and neutral hydrogen density that lead to this temperature were not cited. Definitive temperature measurements will be available from spectroscopic X-ray measurements with *Chandra* (§ 5).

The fitted column density of  $N_{\text{H}} = 5.0 \pm 1.6 \times 10^{20} \text{ atoms cm}^{-2}$  is somewhat higher than the value determined independently from H I radio measurements ( $1.4 \times 10^{20} \text{ atoms cm}^{-2}$ ; Stark et al. 1992). This difference is not highly significant ( $\sim 2.5 \sigma$ ), and may be due to the effective beam sizes for the two measurements of  $N_{\text{H}}$ ; the Stark et al. (1992) survey used a large beam ( $2^\circ$  FWHM), while the X-rays effectively sample a column through the Galaxy only a few arcminutes in radius. This difference may also be due to the contribution of nonneutral hydrogen and other elements to the photoelectric absorption of the low-energy photons from which we determine the column density. It is important to ascertain an accurate column density in order to

TABLE 1  
ASCA SIS/GIS OBSERVING INFORMATION

Detector	Aperture Radius (arcmin)	Source Count Rates ( $\text{s}^{-1}$ )	Useful Exposure Time (s)
SIS0 .....	4.0	0.0925	23,181
SIS1 .....	4.0	0.0750	23,948
GIS2 .....	5.4	0.0532	27,282
GIS3 .....	5.4	0.0672	27,282

TABLE 2  
JOINT ASCA SIS/GIS SPECTRAL MODEL FIT

Parameter	Fitted Value	Uncertainty <sup>a</sup>
$kT_e$ (keV) <sup>b</sup> .....	8.59	+0.86 -0.67
[Fe]/[H] <sup>c</sup> .....	0.14	+0.07 -0.07
$N_{\text{H}}$ ( $10^{20} \text{ atoms cm}^{-2}$ ) .....	5.0	+1.6 -1.6

<sup>a</sup> 68% Confidence interval.

<sup>b</sup> Source frame for  $z = 0.322$ .

<sup>c</sup> Relative to solar  $[\text{Fe}]/[\text{H}] = 4.68 \times 10^{-5}$ .

correctly calculate the X-ray emissivity for the HRI, which is sensitive to energies at which X-ray absorption is significant.

We calculate the X-ray emissivity (Rybicki & Lightman 1979; Sarazin 1988) using the method described by Hughes & Birkinshaw (1998), which is based on a standard thermal plasma code (Raymond & Smith 1977) modified to include relativistic corrections (Gould 1980; Hughes & Birkinshaw 1998). These modifications include the relativistic corrections to the electron distribution function, first-order corrections to the nonrelativistic Born approximation, and first-order corrections from spin and relativistic effects to the electron-ion bremsstrahlung cross section. In addition, the emission from electron-electron bremsstrahlung is included. We calculate the integrated emissivity for the HRI by simulating a thermal source using the temperature and abundance listed in Table 2. We then transform that spectrum to the detector frame, accounting for the redshift of photon energy and for the effects of galactic absorption (Balucinska-Church & McCammon 1992) and the response of the telescope plus mirror combination. Finally, we integrate over the entire HRI energy band ( $\sim 0.5$ – $2.0$  keV). This relativistic calculation yields an integrated emissivity<sup>4</sup> of  $\epsilon = 1.195^{+0.095}_{-0.073} \times 10^{-13} n_e^2$  HRI counts  $\text{cm}^5 \text{s}^{-1}$ . We find the nonrelativistic value to be  $1.142 \times 10^{-13} n_e^2$  HRI counts  $\text{cm}^5 \text{s}^{-1}$ . The uncertainty in the emissivity is derived using the range of parameter values quoted in Table 2; the dominant factor is the uncertainty in the neutral hydrogen column density.

We note that three X-ray point sources are visible within  $\sim 1.5$  of the cluster center in the *ROSAT* HRI image of the Abell 1995 field (Fig. 1a), and thus contribute to the flux measured with the broad *ASCA* beam ( $\sim 3/3$  half-power diameter). The total flux of all three X-ray point sources visible in Figure 1 is 255 HRI counts, which amounts to 13% of the total flux from the cluster (1911 HRI counts). If the ratio of point source to cluster flux is also 13% in the higher energy *ASCA* bandpass, the point sources will have little effect on the temperature derived from the *ASCA* data. If the point sources have power-law spectra typical of active galactic nuclei (AGNs;  $\nu^{-1}$  or steeper), their contribution to the cluster emission in the higher energy *ASCA* bandpass (Fig. 3) will be even less significant. To fully eliminate this ambiguity and to obtain a definitive electron temperature measurement, we have scheduled high angular resolution X-ray spectroscopic measurements of Abell 1995 with *Chandra*, as described in § 5.

### 2.3. Sunyaev-Zeldovich Effect Imaging

The SZE in Abell 1995 was observed interferometrically using the Owens Valley Radio Observatory (OVRO) and Berkeley-Illinois-Maryland Association (BIMA) millimeter arrays, both of which were outfitted with sensitive centimeter-wave receivers optimized for SZE measurements (Carlstrom, Joy, & Grego 1996).

The OVRO observations were obtained in 1996 using six 10.4 m diameter antennas, with baselines ranging from 1.0 to 11.2 k $\lambda$ . The array configuration contained a wide range of baselines, which allowed us to simultaneously image the diffuse SZ decrement (using primarily the short baselines)

and create a high-resolution map of the contaminating point sources in the field (using the long-baseline data). The cluster was observed for a total of eight tracks, with a total on-source integration time of 57.6 hr. The primary beam of the OVRO system can be approximated as Gaussian, with a FWHM of 4.2. The MMA analysis package (Scoville et al. 1993) was used to calibrate and edit the visibility data, which was then output in UVFITS format.

The BIMA observations were made in 1998 with nine 6.1 meter antennas in a very closely packed configuration to maximize sensitivity to the SZE, with baselines ranging from 0.6 to 8.9 k $\lambda$ . The total on-source integration time was 49.6 hr. The primary beam of the BIMA system can be approximated as a Gaussian with a FWHM of 6.6. The MIRIAD software package (Wright & Sault 1993) was used to calibrate and edit the visibility data and then output it in UVFITS format.

We flagged data from baselines when one of the telescopes was shadowed by another telescope in the array, cluster data that were not bracketed in time by phase calibrator data (mostly at the end or beginning of a track), or data for which the phase calibrator indicated poor atmospheric coherence, and, rarely, data with spurious correlations. The 28.5 GHz images were deconvolved (CLEANed) using DIFMAP (Shepherd, Pearson, & Taylor 1994).

In order to properly model the cluster, we must account for any point sources in the field. OVRO's larger dishes and longer telescope separations yield better point-source sensitivity than BIMA. In order to find point sources in the Abell 1995 field, we use DIFMAP to produce a high-resolution OVRO image using only the data with baselines greater than 2 k $\lambda$ . This results in a map with an rms noise of 60  $\mu\text{Jy}$  beam<sup>-1</sup> and a synthesized beam with a FWHM of 17"  $\times$  20". A point source, seen in Figure 4, is detected 34".9 from the cluster pointing center with a statistical significance of 9.7  $\sigma$ . By simultaneously modeling the SZE and the point-source signal in the ( $u, v$ ) plane we find a point-source flux of  $0.58 \pm 0.06$  mJy at 28.5 GHz and  $0.46 \pm 0.07$  mJy at 30.0 GHz. This point source is coincident with a source found in the 1.4 GHz NRAO/VLA Sky Survey (NVSS; Condon et al. 1998) and in the 0.325 GHz Westerbork Northern Sky Survey (WENSS; Rengelink et al. 1997); the measurements are summarized in Table 3. Using BIMA data with baselines greater than 2 k $\lambda$ , we generate a map with a FWHM synthesized beam size of 17".3  $\times$  20".5 and an rms noise of  $\sigma_{\text{rms}} = 130 \mu\text{Jy}$  beam<sup>-1</sup>. At the well-established position, the point source is only marginally detectable in the lower resolution BIMA data, with a flux of  $0.45 \pm 0.13$  mJy at 28.5 GHz, so the OVRO point-source flux was adopted for subsequent analysis of the SZE data.

Quantitative analysis is done by model fitting to the interferometric data directly in the Fourier ( $u, v$ ) plane, where the noise characteristics and the spatial filtering of the interferometer are well understood. A CLEANed image of the SZE decrement toward Abell 1995 measured at OVRO is shown in Figure 1b. This image was created with DIFMAP by applying a Gaussian ( $u, v$ ) taper with a half-power point at 2 k $\lambda$  to stress the large angular scales subtended by the cluster of galaxies before deconvolving the SZE image. The restoring beam for this map has a Gaussian FWHM of 52"  $\times$  59" and an rms noise of 55  $\mu\text{Jy}$  beam<sup>-1</sup>, corresponding to a Rayleigh-Jeans (RJ) brightness sensitivity of  $\sim 27$   $\mu\text{K}$ . The CLEANed image shown in Figure 1b provides an

<sup>4</sup> The factor  $\epsilon$  used here is related to the integrated cooling function  $\Lambda$  used by Hughes & Birkinshaw (1998) and Birkinshaw (1999) by  $\epsilon = \Lambda n_e^2$ .

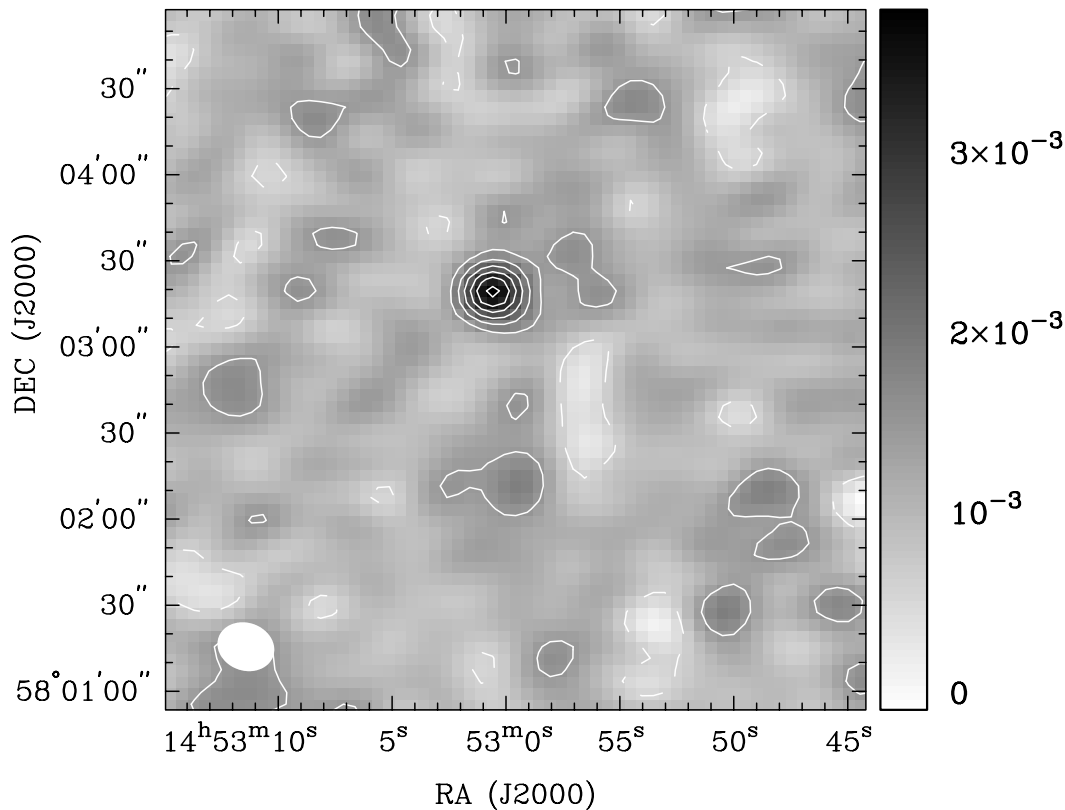


FIG. 4.—Radio point source observed by OVRO at 28.5 GHz. Data with  $(u, v)$  radii greater than  $2 \text{ k}\lambda$  were used to produce this image; the synthesized beam size is  $16''.7 \times 20''.2$ . The contours are in  $1.5 \sigma$  intervals, with the lowest contour at  $-3.0 \sigma$  (with the exception of the zero-level contour, which is not plotted) and the gray-scale units are in  $\text{Jy beam}^{-1}$ . The rms noise of the map is  $\sigma_{\text{rms}} = 60 \mu\text{Jy beam}^{-1}$ .

indicator of the data quality, but the image itself is not used in the analyses.

To constrain the intracluster gas parameters, we fit a  $\beta$ -model plus a point source to the visibility data in the  $(u, v)$  plane (where the interferometric measurements are actually made), rather than in the image plane. To accomplish this, the projected decrement profile predicted from the  $\beta$  model is multiplied by the primary beam and then Fourier transformed to the  $(u, v)$  plane. The transformed model is then fitted simultaneously to the OVRO and BIMA SZE data using the same downhill simplex method employed in § 2 by maximizing the Gaussian likelihood (Reese et al. 2000). The SZE results reported in this paper are given in terms of

decrements in the CMB temperature. To convert to RJ temperatures, divide by 1.021.

The best-fit thermodynamic SZE central decrement, evaluated with the best-fit  $\beta$  model parameters derived from the X-ray fits, is  $\Delta T_0 = -1101 \pm 58 \mu\text{K}$ , where the uncertainties reflect the 68% confidence interval ( $\Delta\chi^2 = 1$ ) derived from the fit to the SZE data. To determine the range of  $\theta_c$ ,  $\beta$  values for which acceptable fits to the SZE data can be obtained, we performed the SZE fits at the same  $\theta_c$ ,  $\beta$  grid points used in the X-ray image analysis (§ 2.1), in the range  $0.50 \leq \beta \leq 0.90$  and  $18'' \leq \theta_c \leq 60''$ . We find that the X-ray data place tighter constraints on the  $\beta$  model than the SZE data do; therefore, in the cluster distance and mass

TABLE 3  
POINT SOURCE FLUX AND POSITION

Observatory	Frequency (GHz)	Flux <sup>a</sup> (mJy)	$\alpha$ (J2000)	$\delta$ (J2000)	Positional Uncertainty (arcsec)
OVRO <sup>b</sup> .....	28.5	$0.58 \pm 0.06$	14 53 00.5	58 03 18.6	$\pm 3$
	30.0	$0.46 \pm 0.07$	14 53 00.5	58 03 18.6	$\pm 3$
NVSS <sup>c</sup> .....	1.4	$8.9 \pm 0.9$	14 53 00.4	58 03 14.1	$\pm 2.5$
WENSS <sup>d</sup> .....	0.325	$34 \pm 3.6$	14 52 59.5	58 03 13.1	$\pm 3.8$

NOTE.—Units of right ascension are hours, minutes, and seconds, and units of declination are degrees, arcminutes, and arcseconds.

<sup>a</sup> The reported OVRO fluxes have been corrected for the response of the primary beam. At an offset of  $34''.9$  from the pointing center, the response of the OVRO primary beam is 0.95.

<sup>b</sup> Point-source position determined using both the 28.5 and 30.0 GHz OVRO observations.

<sup>c</sup> Condon et al. 1996.

<sup>d</sup> Rengelink et al. 1997.

TABLE 4  
ABELL 1995: GALAXY VELOCITIES AND REDSHIFTS

Identification Number	$\alpha$ (J2000)	$\delta$ (J2000)	Velocity ( $cz$ ) (km s $^{-1}$ )	Uncertainties <sup>a</sup> (km s $^{-1}$ )
1.....	14 52 47.86	58 2 1.00	94,015	$\pm 111$
2.....	14 52 53.32	58 2 17.70	93,924	$\pm 106$
3.....	14 52 50.06	58 1 35.50	96,177	$\pm 144$
4 <sup>b</sup> .....	14 52 57.19	58 2 31.60	84,597	$\pm 154$
5 <sup>c</sup> .....	14 52 57.45	58 2 55.20	96,275	$\pm 104$
6.....	14 53 2.31	58 2 49.30	98,341	$\pm 112$
7.....	14 53 1.43	58 3 24.70	96,100	$\pm 108$
8.....	14 53 2.23	58 3 46.50	96,015	$\pm 133$
9.....	14 53 4.02	58 4 3.70	98,334	$\pm 114$
10.....	14 52 51.97	58 2 10.00	98,187	$\pm 104$
11.....	14 52 57.66	58 2 6.40	98,679	$\pm 115$
12.....	14 52 52.94	58 3 25.00	95,041	$\pm 126$
13.....	14 53 0.46	58 3 18.50	97,568	$\pm 135$
14.....	14 52 58.36	58 3 46.40	94,665	$\pm 166$
15.....	14 53 3.73	58 3 33.10	98,145	$\pm 104$
16.....	14 53 4.34	58 3 39.50	95,897	$\pm 136$

NOTE.—Units of right ascension are hours, minutes, and seconds, and units of declination are degrees, arcminutes, and arcseconds.

<sup>a</sup> Presented here are 1  $\sigma$  errors combined in quadrature.

<sup>b</sup> Likely outlier.

<sup>c</sup> A velocity of  $cz = 95,905 \pm 300$  km s $^{-1}$  was previously measured for this galaxy by Huchra et al. 1990.

estimates that follow, we use the X-ray data to constrain  $\theta_c$  and  $\beta$ .

#### 2.4. Optical Spectroscopy of Cluster Galaxies

Twenty spectra of galaxies toward Abell 1995 were obtained during a 1996 June observing run at the Multiple Mirror Telescope (MMT). The telescope was equipped with the red channel spectrograph (Schmidt, Weymann, & Foltz 1989) and a 270 lines mm $^{-1}$  grating, which provided a spectral resolution of  $\sim 3.2$  Å pixel $^{-1}$  over the nominal spectral range of 3800–7400 Å. Spectra of multiple objects were obtained using a set of custom-made aperture plates (Fabricant, McClintock, & Bautz 1991). For this run, we obtained data from two plates, each of which contained spectroscopic slits for 10 candidate galaxies. The positions of the spectroscopic targets were determined from an R-band image of Abell 1995 (Fig. 1c) obtained at the Whipple Observatory 1.2 m telescope in 1996 January.

The total exposure time for each galaxy was 5400 s, split into two equal length exposures to avoid excessive contamination by cosmic rays. We traced and extracted the one-dimensional He-Ne-Ar arc lamp comparison spectra and the sky-subtracted galaxy spectra from each individual frame using the IRAF task *apextract*. The tracing of the spectra had an rms residual of  $\sim 1$  pixel. The arc lamp spectra were wavelength calibrated by identifying at least 30 spectral lines and fitting their positions with a third-order polynomial. Wavelength solutions had typical rms residuals  $\sim 1$  Å ( $\sim 50$  km s $^{-1}$ ). Subsequently, we coadded the spectra from the individual frames and computed the galaxy recessional velocities with the IRAF task *rvsao* by cross-correlating the observed spectra with a high signal-to-noise ratio template spectrum generated for the CfA redshift survey. We estimated our total velocity uncertainty by adding in quadrature the formal cross-correlation error, as provided by *rvsao*, with our estimates for the errors due to sky subtraction and the arc lamp wavelength calibration

( $\sim 50$  km s $^{-1}$ ). The sky-subtraction errors ( $\sim 45$  km s $^{-1}$ ) were estimated by comparing the velocities resulting from using slightly different parameters for the sky fit. As an additional check, we measured the wavelengths of a few selected night-sky emission lines in the spectra and found them to be consistent within the quoted errors ( $\sim 100$  km s $^{-1}$ ) with their expected wavelengths.

Of the 20 objects that we observed in the Abell 1995 field of view, we obtained good S/N spectra for 16 galaxies. The brightest galaxy in the center of the cluster (cluster 5 in Table 4) was one of the two galaxies previously observed by Huchra et al. (1990); the measured velocities for this galaxy agree within the 1  $\sigma$  uncertainties. Fifteen galaxies are likely cluster members (see Table 4), based on a 3  $\sigma$  criteria for rejecting outliers (Yahil & Vidal 1977). Because of the small number of galaxies in our sample, we replaced the classical statistical estimators for the mean and dispersion with more robust biweight estimators (Danese, De Zotti, & di Tullio 1980; Beers et al. 1990, 1991). The mean recessional velocity ( $cz$ ) for these galaxies is  $96,505_{-377}^{+422}$  km s $^{-1}$ , which corresponds to  $z = 0.322 \pm 0.001$  and the (relativistically corrected) velocity dispersion is  $\sigma_v = 1282_{-120}^{+153}$  km s $^{-1}$ . The velocity dispersion is rather high, but consistent with the observed relationship between cluster temperature and  $\sigma_v$  (Girardi et al. 1996).

### 3. CLUSTER DISTANCE AND $H_0$

#### 3.1. Cluster Distance Derived from SZE and X-Ray Data

We estimate the cluster distance from the 28.5 GHz SZE measurement combined with *ROSAT* and *ASCA* X-ray observations of Abell 1995. The expressions for the X-ray surface brightness (in the detector-based units of counts s $^{-1}$  arcmin $^{-2}$ ) and the SZE temperature decrement are given by Birkinshaw (1999):

$$S_X = \frac{1}{4\pi(1+z)^3} \int \epsilon(T_e, n_e) dl, \quad (3)$$

$$\Delta T = f(x) T_{\text{CMB}} \frac{\sigma_T k_B}{m_e c^2} \int n_e T_e dl, \quad (4)$$

where  $n_e$  is the electron number density,  $z$  is the cluster redshift,  $T_{\text{CMB}}$  ( $= 2.728$  K; Fixsen et al. 1996) is the temperature of the CMB radiation,  $\sigma_T$  is the Thomson cross section,  $k_B$  is the Boltzmann constant,  $m_e$  is the electron mass,  $c$  is the speed of light,  $T_e$  is electron gas temperature,  $\epsilon$  is the total X-ray emissivity in the HRI energy band (see § 2.2),  $f(x)$  is the frequency dependence of the SZE, and  $dl$  is the differential length element along the line of sight.

In the nonrelativistic limit, the frequency dependence for the thermodynamic SZE temperature decrement is given by<sup>5</sup>

$$f_{\text{nr}}(x) = x \left( \frac{e^x + 1}{e^x - 1} \right) - 4, \quad (5)$$

where  $x = hv/k_B T_{\text{CMB}}$ ,  $h$  is Planck's constant, and  $\nu$  is the radio observation frequency. At our observing frequency of 28.5 GHz, we find  $f_{\text{nr}}(x) = -1.958$ . After including the

<sup>5</sup> Equation (5) is valid for a temperature decrement expressed as a thermodynamic temperature; for Rayleigh-Jeans temperatures a correction factor of  $x^2 e^x / (e^x - 1)^2$  is present (Rephaeli & Yankovitch 1997; Itoh et al. 1998).

relativistic corrections to the SZE calculated by Itoh, Kohyama, & Nozawa (1998), the leading expression becomes  $f_{\text{rel}}(x, T_e) = -1.899$  at 28.5 GHz.

Solving equations (1)–(4) for the angular diameter distance,  $D_A$  (Hughes & Birkinshaw 1998, eq. [5]), and the central electron number density,  $n_{e0}$ , we find

$$D_A = \left( \frac{\Delta T_0}{A_2} \right)^2 \frac{A_1}{S_{X0}}, \quad (6)$$

$$n_{e0} = \sqrt{\frac{S_{X0}}{A_1 D_A}}, \quad (7)$$

where

$$A_1 = \frac{1}{4\pi(1+z)^3} \frac{\epsilon_0}{n_{e0}^2} \sqrt{\pi} \frac{\Gamma(3\beta - 1/2)}{\Gamma(3\beta)} \theta_c, \quad (8)$$

$$A_2 = f_{\text{rel}}(x, T_e) T_{\text{CMB}} \sigma_T \frac{k_B T_e}{m_e c^2} \sqrt{\pi} \frac{\Gamma(3\beta/2 - 1/2)}{\Gamma(3\beta/2)} \theta_c. \quad (9)$$

Evaluating equation (6) with the parameters derived in § 2, we find  $D_A = 1294$  Mpc. Using this calculated distance and equation (7), we determine the central electron density to be  $n_{e0} = 8.54 \times 10^{-3} \text{ cm}^{-3}$  ( $= 1.23 \times 10^{-2} h^{1/2} \text{ cm}^{-3}$ ). Statistical and systematic uncertainties in  $D_A$  are discussed in § 3.3.

### 3.2. Hubble Constant

A measure of the Hubble constant can be derived from the cluster distance calculated above. For moderate- and high-redshift clusters, the derived  $H_0$  depends on the chosen cosmological model; for the general case of a nonzero cosmological constant,  $H_0$  can be determined from the integral given by Carroll, Press, & Turner (1992, eq. [25]).

We calculate  $H_0$  from the Abell 1995 data using three different cosmological models:

$$H_0 = 45.6 \text{ km s}^{-1} \text{ Mpc}^{-1} \text{ for } \Omega_M = 1.0, \Omega_\Lambda = 0.0.$$

$$H_0 = 48.2 \text{ km s}^{-1} \text{ Mpc}^{-1} \text{ for } \Omega_M = 0.3, \Omega_\Lambda = 0.0.$$

$$H_0 = 52.2 \text{ km s}^{-1} \text{ Mpc}^{-1} \text{ for } \Omega_M = 0.3, \Omega_\Lambda = 0.7.$$

The  $H_0$  values derived for these different cosmologies have a relatively small spread of  $6.6 \text{ km s}^{-1} \text{ Mpc}^{-1}$ .

Figure 5 shows the  $H_0$  values calculated for the  $\Omega_M = 0.3$ ,  $\Omega_\Lambda = 0.7$  case, superimposed on the  $\Delta\chi^2$  contours derived from the  $\beta$  modeling of the HRI X-ray data. The statistical constraints on  $\theta_c$  and  $\beta$  tightly constrain the derived  $H_0$  values, as shown in Figure 5 and Table 5. Other sources of statistical and systematic uncertainty are discussed in § 3.3.

### 3.3. Statistical and Systematic Uncertainties

We now discuss sources of error in the cluster distance calculation, including the uncertainties associated with  $\beta$  model-derived parameters, X-ray temperature, SZE and *ROSAT* absolute flux calibration, contamination from radio point sources, projection effects, temperature gradients, and clumping. The uncertainties are summarized in Table 5.

The statistical variations in the  $\beta$ -model parameters over the allowed range of  $\theta_c$  and  $\beta$  produce an uncertainty in  $D_A$  of  $\pm_{38}^{38}$  Mpc at the 68% confidence. There is also an uncertainty in the normalizations,  $S_{X0}$  and  $\Delta T_0$ , at any given  $(\theta_c, \beta)$  point. At the best-fit  $\theta_c$  and  $\beta$ , this results in an uncertainty in  $D_A$  of  $\pm_{41}^{38}$  Mpc due to fitting errors in  $S_{X0}$  and of  $\pm 136$  Mpc due to fitting errors in  $\Delta T_0$ .

From the X-ray spectral analysis discussion of § 2, we find that the uncertainties in the spectral parameters (electron

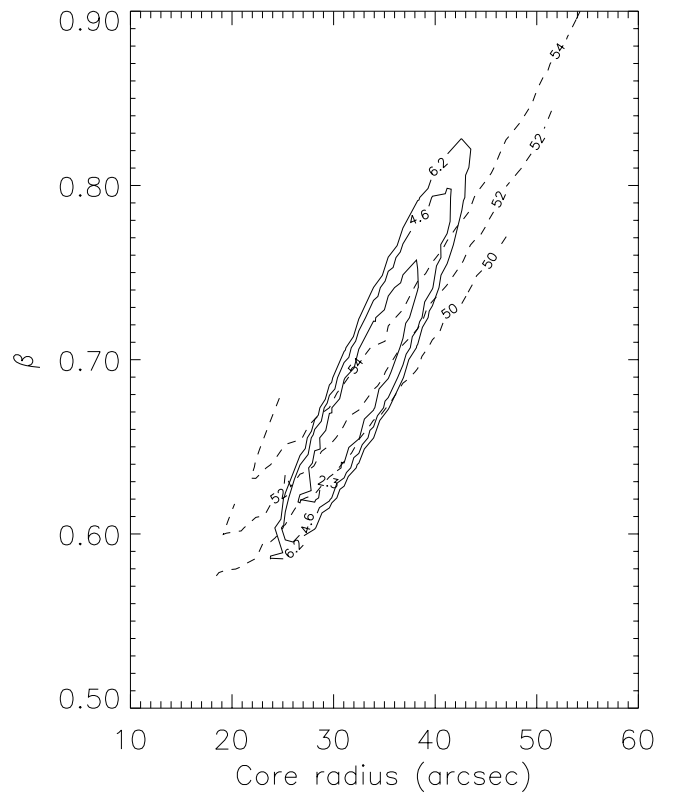


FIG. 5.—Calculated Hubble constant values for Abell 1995, superposed on  $\beta$ -model error bounds. Hubble constant contours (dashed lines) are at 50, 52, and 54  $\text{km s}^{-1} \text{ Mpc}^{-1}$ , and the  $\beta$ -model uncertainty contours correspond to  $\Delta\chi^2 = 2.3, 4.6,$  and  $6.2$ .

temperature, galactic hydrogen column density, metallicity of the cluster gas) collaborate to produce a combined uncertainty range in  $D_A$  of  $\pm_{235}^{256}$  Mpc at 68% confidence. (The cluster distance depends strongly on the measured temperature and emissivity, as indicated in eqs. [6] and [9].)

Another source of error is the systematic uncertainty in the absolute calibration of the X-ray and SZE measurements. The uncertainty of the *ROSAT* HRI absolute X-ray flux calibration is estimated to be  $\pm 15\%$ , which results in a  $\pm 15\%$  uncertainty in  $D_A$  and  $H_0$ . The uncertainty in the absolute calibration of the 28.5 GHz SZE measurements is estimated to be  $\pm 4\%$  by Grego (1998), which results in a  $\pm 8\%$  uncertainty in  $D_A$  and  $H_0$ .

Radio point sources near the cluster center can bias the SZE measurement in two ways:

1. Although the interferometer is effective at measuring and removing point sources (see § 2.3), the uncertainty in the subtracted point-source flux is a source of error in the measurement of the central temperature decrement. To quantify this uncertainty, we varied the point-source flux in the SZE model throughout the 68% confidence interval allowed by the SZE data. We find that the uncertainty in the flux of the known point source results in a  $\sim 2\%$  uncertainty in the SZE decrement ( $\sim 4\%$  in  $D_A$  and  $H_0$ , as shown in Table 5).

2. Undetected radio point source(s) in the Abell 1995 field can introduce a systematic error in our measurement of the SZE. We evaluated this uncertainty by inserting a point source into the cluster model at different positions, starting at the cluster center ( $r = 0''$ ) and going out to a radius of  $80''$ , which includes both the cluster core and the side lobes of the synthesized beam. At each position, we

TABLE 5  
UNCERTAINTY IN DISTANCE AND  $H_0$  ESTIMATES

Source of Error	$\delta D_A$ (Mpc)	$\delta H_0$ (km s <sup>-1</sup> Mpc <sup>-1</sup> )
Statistical Uncertainty		
$\beta$ model <sup>a</sup> .....	+38	+2.2
$S_{X0}$ <sup>b</sup> .....	+38	+1.6
SZE decrement <sup>c</sup> .....	-41	-1.5
X-ray spectral model <sup>d</sup> .....	$\pm 136$	$\pm 5.5$
28.5 GHz point-source flux .....	+256	+9.5
Combined statistical uncertainty .....	-235	-10.3
	+30	+2.4
	-60	-1.2
	+297	+11.6
	-286	-12.0
Systematic Uncertainty		
Absolute X-ray flux calibration .....	$\pm 194$	$\pm 7.8$
Absolute SZE flux calibration .....	$\pm 104$	$\pm 4.2$
Undetected 28.5 GHz point sources .....	+225	+0.6
Peculiar velocity <sup>e</sup> .....	-15	-9.1
Asphericity .....	$\pm 78$	$\pm 3.1$
Clumping and thermal structure .....	+142	+12.0
Combined systematic uncertainty .....	-298	-5.7
	$\pm 259$	$\pm 10.4$
	+438	+18.5
	-459	-17.7

<sup>a</sup> Statistical error (68% confidence interval) due to variations in the model over allowed values of  $\theta_c$  and  $\beta$ .

<sup>b</sup> Statistical uncertainty in modeling central X-ray surface brightness,  $S_{X0}$  (68% confidence interval).

<sup>c</sup> Statistical uncertainty in modeling SZE central decrement (68% confidence interval).

<sup>d</sup> Statistical uncertainty in modeling X-ray spectral data (68% confidence interval).

<sup>e</sup> Assuming a line of sight peculiar velocity of  $v_r = \pm 300$  km s<sup>-1</sup>.

allowed the flux of the introduced point source to vary in the SZE model, and determined the 68% ( $\Delta\chi^2 = 1$ ) confidence interval that was allowed by the SZE data. A 0.1 mJy point source near the cluster center produced the largest increase in the magnitude of the SZE decrement ( $\sim 8.7\%$ ); a 0.03 mJy point source placed in the side lobe at a radius of  $80''$  produces a slight decrease in the magnitude of the decrement ( $\sim 0.5\%$ ). We adopt these errors ( $^{+8.7}_{-0.5}\%$ ) as the  $1\sigma$  uncertainties in the decrement due to the presence of an undetected point source. The resulting uncertainties in  $D_A$  and  $H_0$  are reported in Table 5. A more sensitive point-source survey is planned, which will reduce the magnitude of this systematic uncertainty.

We now consider the effects of cluster ellipticity and projection on the cluster distance determination. Fitting an elliptical isothermal  $\beta$  model to the HRI data gives a best-fit observed axial ratio of  $a/b = 1.42$ . Because of possible projection effects, the measured value represents a lower limit to the intrinsic cluster ellipticity. Based on the cluster ellipticity distribution reported by Mohr et al. (1995), we estimate an upper limit to the intrinsic cluster ellipticity of  $a/b = 2.0$ . Projected ellipsoidal  $\beta$  models (Hughes & Birkinshaw 1998) are used to determine the range of  $H_0$  values that are consistent with the observed axis ratio and the limits on intrinsic ellipticity. We find that  $H_0$  can be overestimated by as much as 11% if the cluster is prolate, and that  $H_0$  can be underestimated by as much as 23% if the cluster is oblate. We adopt these percentages as the  $1\sigma$  uncertainties due to the effects of cluster ellipticity and projection.

When averaged over a sample of clusters, however, the distance-scale uncertainties are much smaller: using a sample of 25 simulated triaxial clusters with an ellipticity distribution consistent with the Mohr et al. (1995) measure-

ments, Sulkanen (1999) found that the mean  $H_0$  value is within  $\sim 7\%$  of the true value at 68% confidence. An accurate determination of  $H_0$  will require X-ray and SZE measurements for a large sample of clusters, an effort that is currently underway (van Speybroeck 1987, 1999; Myers et al. 1997; Reese et al. 2000).

The change in the CMB temperature due to the radial peculiar velocity of the cluster (the kinematic Sunyaev-Zeldovich Effect; Sunyaev & Zeldovich 1980) can introduce a modest error into the measurement of the thermal SZE. For a value of the radial peculiar velocity of  $300$  km s<sup>-1</sup> and using the cluster gas temperature found in § 2.2, an error of  $\pm 6\%$  is introduced in the distance (Birkinshaw 1999). As with the effects of cluster geometry and orientation, measurements of a sample of clusters will reduce this error substantially.

The existence of temperature gradients or clumping in the cluster gas distribution can lead to systematic errors in our distance determination. On large angular scales, initial observational work suggested that steep declining temperature gradients might be prevalent in galaxy clusters (Markevitch et al. 1998); however, recent studies are consistent with an isothermal temperature distribution (Irwin, Bregman, & Evrard 1999; White 2000). To quantitatively assess the impact that large-scale temperature gradients may have on the distance determination, it is essential to fully account for the observing technique (e.g., Holzapfel et al. 1997). J. J. Mohr et al. (in preparation) have performed extensive cluster simulations, including the response of our interferometric instrument. Their analysis indicates that large-scale cluster temperature gradients introduce very little systematic error in the cluster distance, because both the interferometric SZE observations and the X-ray emission are dominated by gas within a few core radii, and are insensitive to cool gas that may exist at large radii. Regarding small-scale clumping within the intracluster medium (ICM), J. J. Mohr et al. (in preparation) find that clumping due to subcluster merging does enhance the X-ray surface brightness by  $\sim 20\%$ , causing X-ray gas mass estimates to be overestimated by 10% and the cluster distance to be underestimated by  $\sim 20\%$ . There is currently no direct observational evidence of clumping within the ICM, but merger signatures are common (Mohr et al. 1995), and mergers are the driving mechanism behind these fluctuations in the simulated clusters (Mathiesen, Evrard, & Mohr 1999). We conservatively include a 20% systematic uncertainty due to the combined effects of clumping and departures from isothermality.

On small angular scales, a cooling flow in the center of a cluster can bias the derived X-ray surface brightness and temperature, but in the case of Abell 1995 we find no significant excess in the HRI surface brightness profile and hence no specific indication of a cooling flow: the peak X-ray flux measured at the cluster center,  $S_{X0} = 0.039 \pm 0.008$  counts s<sup>-1</sup> arcmin<sup>-2</sup>, differs by less than  $1\sigma$  from the smooth  $\beta$ -model prediction (§ 2.1). Upcoming measurements of Abell 1995 with the X-ray imaging spectrometer on *Chandra*, as discussed in § 5, will address the issue of thermal structure in the cluster and will place strong constraints on the possible contribution of an X-ray cooling flow.

When all the uncertainties are considered, we find  $D_A = 1294^{+294}_{-283} {}^{+483}_{-458}$  Mpc,  $H_0 = 52.2^{+11.4}_{-11.9} {}^{+18.5}_{-17.7}$  km s<sup>-1</sup> Mpc<sup>-1</sup> for  $\Omega_M = 0.3$  and  $\Omega_\Lambda = 0.7$ . The quoted errors (statistical

followed by systematic) have been combined in quadrature from the individual uncertainties shown in Table 5.

#### 4. MASS ANALYSIS

The X-ray and optical data presented in § 2 can be used to derive the total cluster mass, the gas mass, and thus the cluster gas mass fraction. The total mass is found using two independent methods: (1) the equation of hydrostatic equilibrium, coupled with the gas density profile and the electron temperature, and (2) the virial theorem, coupled with the velocity dispersion. The gas mass of the cluster is derived from the X-ray imaging measurements presented in § 2.1.

##### 4.1. Total Cluster Mass

Determining the total cluster mass using the equation of hydrostatic equilibrium requires knowledge of the electron gas density and temperature profiles. Here we assume that the cluster is isothermal and follows a spherical isothermal  $\beta$  model, so that the total mass can be obtained from equation (2) of Evrard, Metzler, & Navarro (1996) using the gas density profile determined in § 2.1, the gas temperature measured in § 2.2, and a mean molecular weight of  $\mu = 0.61$ . Note that the total mass does not depend on the normalization of the gas distribution, but only on the shape parameters. The mass equation is evaluated at a radius of  $r_{500} = 830 h^{-1}$  kpc, where numerical simulations indicate that the hydrostatic assumption is valid (Evrard et al. 1996). From our measured gas density profile and cluster gas temperature, we derive a total mass of  $M_{\text{tot}}^{\text{HSE}}(r_{500}) = 5.18^{+0.62}_{-0.48} \times 10^{14} h^{-1} M_{\odot}$ .

An alternate measure of the total cluster mass can be obtained from the virial theorem, which yields a total mass of  $2\sigma_v^2 rG^{-1}$ , where  $\sigma_v$  is the one-dimensional velocity dispersion (Carlberg et al. 1996). Using the measured velocity dispersion for Abell 1995 (§ 2.4), this method yields a total mass  $M_{\text{tot}}^{\text{virial}}(r_{500}) = 6.35^{+1.51}_{-1.19} \times 10^{14} h^{-1} M_{\odot}$ , in good agreement with the hydrostatic equilibrium calculation above. In subsequent calculations, we use the total mass determined from the X-ray temperature and the assumption of hydrostatic equilibrium.

The uncertainties in the mass calculations are determined by combining in quadrature the modeling of the ROSAT HRI imaging data, the ASCA X-ray spectra, the optical velocity dispersion, and the absolute X-ray flux calibration. For each mass estimate discussed in this section, the uncertainties are itemized in Table 6.

##### 4.2. Gas Mass

To determine the cluster gas mass,  $M_{\text{gas}}$ , we employ the same density profile that was used to calculate the total mass in the hydrostatic case above. The gas mass within a radius  $r_0$  is found by radially integrating the spherically

symmetric density distribution,

$$M_{\text{gas}}(r_0) = 4\pi \left( \frac{\mu n_{\text{tot}}}{n_{e0}} \right) m_{\text{H}} n_{e0} r_c^3 \int_0^{r_0/r_c} (1 + s^2)^{-3\beta/2} s^2 ds, \quad (10)$$

where the integral is expressed in terms of the dimensionless variable  $s \equiv r/r_c$  and the core radius  $r_c = \theta_c D_A$ . The factor  $\mu n_{\text{tot}}/n_{e0}$  is derived using the abundances from Anders & Grevesse (1989) and has the value of 1.165. Inserting the central electron density,  $n_{e0} = 1.23^{+0.20}_{-0.10} \times 10^{-2} h^{1/2} \text{ cm}^{-3}$ ,  $\beta = 0.672^{+0.052}_{-0.035}$ , and  $r_c = 98.3^{+8.8}_{-13.1} h^{-1}$  kpc derived from the X-ray data, we obtain a gas mass of  $M_{\text{gas}}(r_{500}) = 2.90^{+0.25}_{-0.38} \times 10^{13} h^{-5/2} M_{\odot}$ , where the errors reflect the uncertainty in our spatial and spectral modeling of the X-ray data as well as the uncertainty in the absolute X-ray flux calibration (Table 6).

##### 4.3. Gas Mass Fraction and $\Omega_M$

The ratio of gas mass to total mass ( $f_g$ ) in Abell 1995, as determined from the X-ray data in §§ 4.1 and 4.2, is  $f_g = 0.056^{+0.010}_{-0.013} h^{-3/2}$ . The uncertainties are detailed in Table 6. This result is consistent at the  $2\sigma$  level with the X-ray-derived mean gas mass fraction found by Mohr, Mathiesen, & Evrard (1999) using a sample of 28 nearby clusters observed by the ROSAT PSPC, as well as the SZE-derived mean gas mass fraction (Grego et al. 2000; Myers et al. 1997).

The ratio of the gas mass to the total cluster mass is cosmologically significant because, if measured over a sufficiently large volume, the gas mass fraction sets a lower limit on the universal baryon fraction,  $f_B \equiv \Omega_B/\Omega_M$  (White et al. 1993; David, Jones, & Forman 1995; White & Fabian 1995; Briel & Henry 1996; Myers et al. 1997; Mohr et al. 1999; Grego et al. 2000). The gas mass fraction is only a lower bound to the universal baryon fraction, since it does not account for other forms of baryonic matter, such as the luminous matter in galaxies that is known to make up at least  $\sim 10\%$  of the total cluster mass (Forman & Jones 1982; White et al. 1993). Using the baryon density parameter  $\Omega_B = (0.019 \pm 0.002)h^{-2}$  (Burles & Tytler 1998), this lower bound on  $f_B$  in turn yields an upper bound on the universal mass density parameter; from the Abell 1995 data, we derive  $\Omega_M h^{1/2} \leq 0.34^{+0.06}_{-0.05}$ . Stronger constraints have been obtained from measurements of an ensemble of clusters:  $\Omega_M h \leq 0.23^{+0.04}_{-0.05}$  was inferred from SZE measurements of clusters by Grego et al. (2000), and Mohr et al. (1999) use X-ray cluster measurements to derive  $\Omega_M h^{1/2} \leq 0.25 \pm 0.01$ .

## 5. CONCLUSIONS

We present X-ray imaging and spectroscopy, interferometric imaging of the SZE, and optical spectroscopy of the galaxy cluster Abell 1995. The X-ray imaging data were obtained with the ROSAT HRI instrument and the X-ray spectroscopy from the ASCA SIS and GIS instruments. From these data, we infer  $\theta_c = 32'5^{+2'9}_{-4'3}$ ,  $\beta = 0.67^{+0.05}_{-0.03}$ , a central electron number density of  $n_{e0} = 1.23^{+0.20}_{-0.10} \times 10^{-2} h^{1/2} \text{ cm}^{-3}$ , a central X-ray surface brightness of  $S_{X0} = 3.24^{+0.39}_{-0.14} \times 10^{-2} \text{ counts s}^{-1} \text{ arcmin}^{-2}$ , and an electron temperature of  $k_B T_e = 8.59^{+0.80}_{-0.67} \text{ keV}$ . With these results, we calculate a relativistically correct X-ray emissivity over the HRI energy range of  $\epsilon = 1.196^{+0.094}_{-0.074} \times 10^{-13} n_e^2 \text{ HRI counts cm}^5 \text{ s}^{-1}$ . The SZE was interferometrically imaged

TABLE 6

UNCERTAINTY IN MASS AND  $f_g$  ESTIMATES

Source of Error	$\delta M_{\text{tot}}^{\text{vir}}$ (%)	$\delta M_{\text{tot}}^{\text{HSE}}$ (%)	$\delta M_{\text{gas}}$ (%)	$\delta f_g$ (%)
X-ray $\beta$ model .....	...	+7.4	+8.2	+10.6
Spectral model .....	...	-4.9	-12.6	-18.6
Velocity dispersion .....	...	+9.3	+3.2	+11.7
Absolute X-ray flux calibration .....	...	-7.8	-3.7	-12.4
Combined Uncertainty .....	+23.9 -18.7	...	...	...
	...	...	$\pm 7.5$	$\pm 7.5$
	+23.9 -18.7	+11.9 -9.2	+11.6 -15.1	+17.5 -23.6

using the OVRO and BIMA millimeter arrays in compact configurations outfitted with 28.5 GHz receivers optimized for SZE measurements. The central thermodynamic SZE decrement evaluated at the best-fit  $\beta$  model parameters (derived from the HRI X-ray data) is  $\Delta T_0 = -1101 \pm 58 \mu\text{K}$ . We also present optical spectroscopy of the cluster from the MMT, which greatly increases the number of measured galaxy redshifts in this cluster from 2 to 15, yielding a mean cluster redshift of  $0.322^{+0.001}_{-0.001}$  and a velocity dispersion of  $1282^{+153}_{-120} \text{ km s}^{-1}$ .

The X-ray, SZE, and optical results are combined using a spherical isothermal  $\beta$  model to determine the cluster distance  $D_A = 1294^{+294}_{-283} +438_{-458} \text{ Mpc}$ , implying a Hubble constant of  $H_0 = 52.2^{+11.4}_{-11.9} +18.5_{-17.7} \text{ km s}^{-1} \text{ Mpc}^{-1}$  for  $\Omega_M = 0.3$  and  $\Omega_\Lambda = 0.7$ . When additional cosmological models are considered ( $\Omega_M = 1, \Omega_\Lambda = 0$  and  $\Omega_M = 0.3, \Omega_\Lambda = 0$ ), we find that the best-fit  $H_0$  values range from 46 to 52  $\text{km s}^{-1} \text{ Mpc}^{-1}$ . In the distance and  $H_0$  estimate, the first set of errors reflect the statistical uncertainty in modeling the X-ray imaging data, the SZE imaging data, and the X-ray spectral data combined in quadrature. The second set of errors reflect the systematic uncertainties in absolute calibration, undetected 28.5 GHz point sources, kinematic SZE, asphericity, clumping, and deviations from isothermality, combined in quadrature. The systematic errors in  $H_0$  associated with kinematic SZE and asphericity will be substantially reduced when measurements of a sample of clusters are analyzed.

Finally, we use two independent methods to determine the total cluster mass (the equation of hydrostatic equilibrium coupled with the gas density profile and the electron temperature, and the virial theorem coupled with the measured galaxy velocity dispersion), which yield  $M_{\text{tot}}^{\text{HSE}}(r_{500}) = 5.18^{+0.62}_{-0.48} \times 10^{14} h^{-1} M_\odot$  and  $M_{\text{tot}}^{\text{virial}}(r_{500}) = 6.35^{+1.51}_{-1.19} \times 10^{14} h^{-1} M_\odot$ . Based on the X-ray data, the gas mass is found to be  $M_{\text{gas}}(r_{500}) = 2.90^{+0.25}_{-0.38} \times 10^{13} h^{-5/2} M_\odot$ , and the resulting gas mass fraction is  $f_{\text{gas}} = 0.056^{+0.010}_{-0.013} h^{-3/2}$ . In combination with recent baryon density constraints, the measured gas mass fraction yields an upper limit on the mass density parameter of  $\Omega_M h^{1/2} \leq 0.34^{+0.06}_{-0.05}$ .

We will be able to significantly reduce several of the statistical and systematic uncertainties with an upcoming 48 ks observation Abell 1995 with *Chandra*. A major source of uncertainty is the poorly determined X-ray temperature. The *ROSAT* HRI data presented in this paper does not contain any spectral information, and spatially resolved temperature measurements of this cluster are not possible with *ASCA* due to the broad point response function of the *ASCA* telescope. The observation of Abell 1995 with *Chandra's* Advanced CCD Imaging Spectrometer will provide good spectral resolution over a broadband (0.1–10 keV) arcsecond angular resolution, and absolute calibration uncertainties of  $\sim \pm 3\%$ . A total of  $\sim 2 \times 10^4$  counts are predicted for the 48 ks observation, sufficient to constrain the temperature profile of the cluster gas, and to reduce the current uncertainties in the X-ray temperature and the absolute X-ray flux scale by a factor of 5.

This work is supported by NASA LTSA grant number NAG5-7986. Cluster research at Rutgers is partially supported by NASA LTSA grant NAG5-3432. We thank Cheryl Alexander, Rick Forster, Curt Giovanine, Ron Lawrence, Steve Padin, Dick Plambeck, Steve Scott, Mark Warnock, Paul Whitehouse, Dave Woody, and the staff of the OVRO and BIMA observatories for their outstanding support of the interferometric SZE imaging project. We also thank Joseph J. Mohr, Doris Neumann, and Martin Sulkanen for stimulating discussions and valued comments, and S. K. P. and E. D. R. gratefully acknowledge support from NASA GSRP fellowships NGT8-52863 and NGT5-50173. Radio astronomy with the OVRO millimeter array is supported by NSF grant AST 96-13717 and at the BIMA millimeter array by NSF grant AST 96-13998. The funds for the additional hardware for the SZE experiment were from a NASA CDDF grant, a NSF-YI Award, and the David and Lucille Packard Foundation. The X-ray data for this research were obtained through the High Energy Astrophysics Science Archive Research Center, provided by the NASA/Goddard Space Flight Center.

## REFERENCES

- Anders, E., & Grevesse, N. 1989, *Geochim. Cosmochim. Acta*, 53, 197  
 Balucinska-Church, M., & McCammon, D. 1992, *ApJ*, 400, 699  
 Beers, T. C., Flynn, K., & Gebhardt, K. 1990, *AJ*, 100, 32  
 Beers, T. C., Forman, W., Huchra, J. P., Jones, C., & Gebhardt, K. 1991, *AJ*, 102, 1581  
 Birkinshaw, M. 1999, *Phys. Rep.*, 310, 97  
 Briel, U. G., & Henry, J. P. 1996, *ApJ*, 472, 131  
 Burles, S., & Tytler, D. 1998, *ApJ*, 507, 732  
 Carlstrom, J. E., Joy, M., & Grego, L. 1996, *ApJ*, 456, L75  
 Carlberg, R. G., Yee, H. K. C., Ellingson, E., Abraham, R., Gravel, P., Morris, S., & Pritchet, C. J. 1996, *ApJ*, 462, 32  
 Carroll, S. M., Press, W. H., & Turner, E. L. 1992, *ARA&A*, 30, 499  
 Cash, W. 1979, *ApJ*, 228, 939  
 Cavaliere, A., & Fusco-Femiano, R. 1976, *A&A*, 49, 137  
 ———, 1978, *A&A*, 70, 667  
 Condon, J. J., Cotton, W. D., Greisen, E. W., Yin, Q. F., Perley, R. A., Taylor, G. B., & Broderick, J. J. 1998, *AJ*, 115, 1693  
 Danese, L., De Zotti, G., & di Tullio, G. 1980, *A&A*, 82, 322  
 David, L. P., Jones, C., & Forman, W. 1995, *ApJ*, 445, 578  
 David, L. P., et al. 1997, *The ROSAT High-Resolution Imager (HRI) Calibration Report* (Washington: US *ROSAT* Science Data Center, Smithsonian Astrophysical Observatory)  
 Day, C., Arnaud, K., Ebisawa, K., Gotthelf, E., Ingham, J., Mukai, K., & White, N. 1995, *The ABC Guide to ASCA Data Reduction*, 4th Version (*ASCA GOF*)  
 Evrard, A. E., Metzler, C. A., & Navarro, J. F. 1996, *ApJ*, 469, 494  
 Fabricant, D. G., McClintock, J. E., & Bautz, M. W. 1991, *ApJ*, 381, 33  
 Fixsen, D. J., Cheng, E. S., Gales, J. M., Lather, J. C., Schafer, R. A., & Wright, E. L. 1996, *ApJ*, 473, 576  
 Forman, W., & Jones, C. 1982, *ARA&A*, 20, 547  
 Girardi, M., Fadda, D., Giuricin, G., Mardirossian, F., Mezzetti, M., & Biviano, A. 1996, *ApJ*, 457, 61  
 Gould, R. J. 1980, *ApJ*, 238, 1026; erratum 243, 667 (1981)  
 Grego, L. 1998, Ph.D. thesis, California Inst. Technology  
 Grego, L., Carlstrom, J. E., Reese, E. D., Holder, G. P., Holzapfel, W. L., Joy, M., Mohr, J. J., & Patel, S. K. 2000, *ApJ*, submitted  
 Holzapfel, W. L., Arnaud, M., Ade, P. A. R., Church, S. E., Fischer, M. L., Mausekopf, P. D., Rephaeli, Y., Wilbanks, T. M., & Lange, A. E. 1997, *ApJ*, 480, 449  
 Huchra, J. P., Henry, J. P., Postman, M., & Geller, M. J. 1990, *ApJ*, 365, 66  
 Hughes, J. P., & Birkinshaw, M. 1998, *ApJ*, 501, 1  
 Irwin, J. A., Bregman, J. N., & Evrard, A. E. 1999, *ApJ*, 519, 518  
 Itoh, N., Kohyama, Y., & Nozawa, S. 1998, *ApJ*, 502, 7  
 Kendall, M., & Stuart, A. 1979, *The Advanced Theory of Statistics*, Vol. 2 (New York: Macmillan), 246  
 Markevitch, M., Forman, W. R., Sarazin, C. L., & Vikhlinin, A. 1998, *ApJ*, 503, 77  
 Mathiesen, B., Evrard, A. E., & Mohr, J. J. 1999, *ApJ*, 520, L21  
 Mohr, J. J., Evrard, A. E., Fabricant, D. G., & Geller, M. J. 1995, *ApJ*, 447, 8  
 Mohr, J. J., Mathiesen, B., & Evrard, A. E. 1999, *ApJ*, 517, 627  
 Mushotzky, R. F., & Scharf, C. A. 1997, *ApJ*, 482, L13  
 Myers, S. T., Baker, J. E., Readhead, A. C. S., Leitch, E. M., & Herbig, T. 1997, *ApJ*, 485, 1  
 Raymond, J. C., & Smith, B. W. 1977, *ApJS*, 35, 41  
 Reese, E. D., Mohr, J. J., Carlstrom, J. E., Joy, M., Grego, L., Holder, G. P., Holzapfel, W. L., Hughes, J. P., Patel, S. K., & Donahue, M. 2000, *ApJ*, 533, 38  
 Rengelink, R. B., Tang, Y., de Bruyn, A. G., Miley, G. K., Bremer, M. N., Roettgering, H. J. A., & Bremer, M. A. R. 1997, *A&AS*, 124, 259

- Rephaeli, Y. 1995, *ARA&A*, 33, 541  
Rephaeli, Y., & Yankovitch, D. 1997, *ApJ*, 481, L55  
Rybicki, G. B., & Lightman, A. P. 1979, *Radiative Processes in Astrophysics* (New York: Wiley), 160  
Sarazin, C. L. 1988, *X-Ray Emission from Clusters of Galaxies* (Cambridge: Cambridge Univ. Press), 145  
Schmidt, G., Weymann, R., & Foltz, C. 1989, *PASP*, 101, 713  
Scoville, N. Z., Carlstrom, J. E., Chandler, C. J., Phillips, J. A., Scott, S. L., Tilanus, R. P. J., & Wang, Z. 1993, *PASP*, 105, 1482  
Shepherd, M. C., Pearson, T. J., & Taylor, G. B. 1994, *BAAS*, 26, 987  
Stark, A. A., Gammie, C. F., Wilson, R. W., Bally, J., Linke, R. A., Heiles C., & Hurwitz, M. 1992, *ApJS*, 79, 77  
Sulkanen, M. E. 1999, *ApJ*, 522, 59  
Sunyaev, R. A., & Zeldovich, Ya. B. 1972, *Comments Astrophys. Space Phys.*, 4, 173  
———. 1980, *MNRAS*, 190, 413  
Van Speybroeck, L. P. 1987, *Astrophys. Lett. Commun.*, 26, 12  
———. 1999, *BAAS*, 194, 58.12  
White, D. A. 2000, *MNRAS*, in press  
White, D. A., & Fabian A. C. 1995, *MNRAS*, 273, 72  
White, S. D. M., Navarro, J. F., Evrard, A. E., & Frenk, C. S. 1993, *Nature*, 366, 429  
Wright, M. H. C., & Sault, R. J. 1993, *ApJ*, 402, 546  
Yahil, A., & Vidal, N. V. 1977, *ApJ*, 214, 347